JOURNAL OF PROPULSION AND POWER
Vol. 23, No. 5, September–October 2007

System Modeling of Explosively Actuated Valves

Adam M. Braud* and Keith A. Gonthier†
Louisiana State University, Baton Rouge, Louisiana 70803
and
Michele E. Decroix‡
Los Alamos National Laboratory, Los Alamos, New Mexico 87545

DOI: 10.2514/1.27414

A model is formulated to describe time-dependent operation of an explosively actuated valve. The model accounts for burning of solid explosive to form product gas within an actuator, transport of product gas from the actuator to an expansion chamber, and insertion of an initially tapered piston into a constant diameter bore by gas pressure within the expansion chamber. A cutter attached to the piston punctures a diaphragm enabling the desired gas flow. An important model feature is the coupling of combustion energy to piston–housing deformation resulting from gas pressure and geometric interference during piston insertion. The model is correlated with quasi-static compression tests, and combustion bomb data for the explosive HMX ($C_4H_8N_8O_8$), that provide estimates for the valve work requirements, and the pressure dependent burning rate, respectively. The model is then used to predict operation of a baseline valve configuration and to assess how variations in explosive mass and valve geometry affect performance. Predictions indicate that 150 mg of HMX routinely used with the baseline valve induces far greater piston kinetic energy than needed for successful operation. The appropriateness of key assumptions about stress and deformation fields within the piston and housing are examined based on a rate-independent finite-element analysis.

I. Introduction

EXPLOSIVELY and pyrotechnically actuated devices, such as pin pullers, cable cutters, thrusters, and valves, are routinely used to perform critical functions in numerous industrial, aerospace, and defense related applications because they can reliably and safely deliver high power in remote environments by the combustion of a self-contained energy source. Historically, the design of these devices has been largely empirical and considered by some to be an art [1]. There has recently been greater emphasis placed on carefully examining device design and performance in response to a number of spacecraft mishaps (Landsat 6, Telstar 4, and the Mars Observer) that occurred when explosively and pyrotechnically actuated hardware did not properly function [2–5]. Devices were previously qualified based on simple go/no-go tests; if an existing device actuated with an 85% propellant mass load, then the lot of devices was considered suitable for use. More quantitative tests have subsequently been used to characterize device performance such as inert gas gun tests [6]. Though experiments are ultimately needed to assess device performance, it is desirable to formulate inexpensive modeling tools that can facilitate experimentation in the design and development of a new generation devices such as microvalves and thrusters [7–10].

A key objective of this work is to formulate a comprehensive, but simple, mathematical model that can be used to quickly explore and assess the effects of geometric, structural, and energetic material design modifications on the power producing capability and performance of explosively actuated devices in different environments. To this end, we focus on describing the operation and performance of a conventional nitrogen cartridge valve, but emphasize that our model can be easily adapted and applied to other devices such as pin pullers and cable cutters. Here, performance collectively refers to quantities that are typically used to characterize valve operation such as its pressure history, piston velocity history, and piston stroke time.

The axisymmetric valve modeled in this work is shown in Fig. 1 in both its prefired and postfired configurations. Representative valve dimensions are indicated in the figure; other valve dimensions used in this study are given in later sections where appropriate. The purpose of this valve is to enable the flow of stored nitrogen gas through a transfer conduit at a desired time. The valve is driven by the combustion of 150 mg of the solid explosive HMX ($C_4H_8N_8O_8$) contained within a small actuator cartridge that is threaded into the device directly above the product gas expansion chamber. Combustion of the explosive, which is initiated by an embedded hot wire, produces a mixture of high temperature gases that rapidly pressurize the actuator volume. The explosive and combustion products are initially sealed within the actuator by a metal burst disc that facilitates ignition and subsequent combustion by allowing for pressure buildup before rupturing. The burst disc ruptures when the pressure within the actuator exceeds a critical value ($\approx$55 MPa), enabling the flow of product gases (and possibly some unreacted explosive) through the actuator port (3.8 mm diam) and into the expansion chamber where it exerts a net axial force on the open end of the piston pushing it into the valve bore. This movement induces coupled elastic and plastic deformation of the initially tapered, hollow piston skirt and the confining housing, and significant frictional resistance between these components due to mechanical interference. Both the piston and housing are made of stainless steel, where the housing material has been strain hardened for enhanced strength during valve operation; the piston and housing mechanical properties are summarized in Secs. III.B and IV.B. We only consider deformation of the piston skirt, and not the cylindrical, solid part of the piston initially contained within the bore, as experiments and detailed numerical simulations both indicate that it is the major source of resistance to piston motion. The cutter, attached to the closed bottom end of the piston, penetrates the diaphragm as the moving piston is brought to rest by contact with the stops. Valve operation is then complete approximately 90 μs following ignition as stored nitrogen gas flows through the newly created opening into the gas transfer conduit. The total axial displacement of the piston (i.e., stroke length) is approximately 6.3 mm. The original design of

Presented as Paper 3843 at the 41st AIAA/ASME/SAE/ASEE Joint Propulsion Conference and Exhibit, Tucson, Arizona, 10–13 July 2005; received 21 August 2006; revision received 1 February 2007; accepted for publication 30 March 2007.

*Graduate Research Assistant, Mechanical Engineering Department.
†Assistant Professor, Mechanical Engineering Department; gonthier@me.lsu.edu (Corresponding Author).
‡Technical Staff Member, Decision Applications Division.

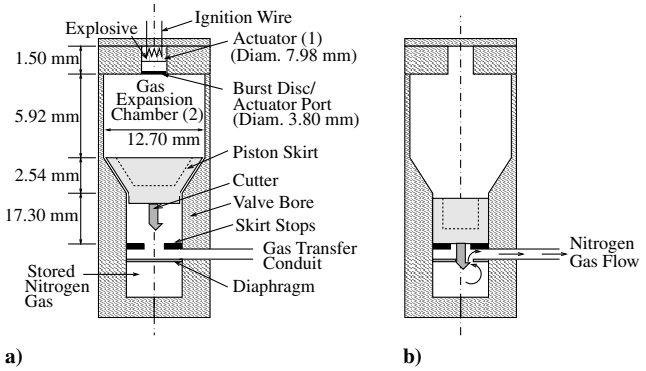

Fig. 1 Schematic of an explosively actuated nitrogen cartridge valve: a) prefired and b) postfired configuration (drawing is not to scale).

this valve, and subsequent modifications, were largely based on limited empirical data. The model formulated in this paper is intended to give designers a predictive capability that enables them to make informed decisions regarding design changes.

There are few modeling studies reported in the open literature on explosively and pyrotechnically driven devices. Importantly these studies give only partial descriptions of device operation. The model described by Jones et al. [11,12], uses analytical and computational results based on pressure vessel theory to estimate the work required to operate an explosively actuated valve. Their model, although useful, does not describe the combustion process and its influence on valve operation, nor does it describe the effects of internal gas pressure or material strain hardening on valve deformation. The model described by Ng and Kwon [13] is similar to the deformation model of Jones et al., but additionally accounts in a simple way for the burning of an explosive with subsequent adiabatic gas expansion; like Jones et al., they do not consider the effect of internal gas pressure or material strain hardening on device deformation. The multiphase model described by Gonthier and Powers [14,15] describes the coupled, time-dependent combustion and work processes required to operate a pyrotechnically actuated pin puller, but does not describe the effect of component material strength and deformation on device performance.

The comprehensive model formulated in this paper combines and extends key features of previous models to account for coupled 1) time-dependent combustion of explosive within the actuator, 2) flow of product gases from the actuator into the expansion chamber, 3) work performed by high pressure combustion gases within the expansion chamber in moving the piston, 4) elastic–plastic deformation of the piston and housing that confines its motion, and 5) frictional resistance due to relative motion between the piston and housing. Features included in this description that have not been previously addressed include the effects of finite-rate explosive energy release, internal gas pressure, and material strain hardening on piston insertion and device performance. Rigorous constitutive theories are sacrificed for tractability when feasible. The model tracks the time-dependent, spatially averaged evolution of explosive and combustion product mass and energy based on principles of mixture theory. Here, it is assumed that combustion products are formed in fixed ratios determined by chemical equilibrium calculations, as assumed by Gonthier et al. [14,15] for the pin puller model. Forcing terms in the product energy equations account for heat and work interactions with the surrounding valve structure. The work interactions are coupled to an equation of motion for the piston that accounts for axial resistance with the valve bore due to coupled piston and housing deformation. As in the work of Jones et al. [11,12], we assume that the spatial stress field within the piston and housing locally equilibrates during the device operation time enabling leading-order estimates for valve performance to be obtained; as such, the deformation is considered quasi static. Both inert compression tests and finite-element analysis (FEA) are performed to characterize the quasi-static force and energy requirements of the valve, and the deformation and stress fields within the piston and housing, respectively, which collectively facilitate development of the comprehensive model. The comprehensive model is constructed so that the total system mass and energy are conserved. Other key assumptions are given in appropriate sections of this paper.

An outline of this paper is as follows. Summarized in Sec. II is a model for the evolution of explosive and combustion product mass and thermal energy within the actuator and gas expansion chamber, and a model for piston motion and valve deformation. Section III gives comparisons between inert model predictions, quasi-static compression tests, and finite-element predictions for the force and work needed to insert the piston into the valve bore and puncture the diaphragm. The model is then used in Sec. IV to describe the operation of the baseline nitrogen cartridge valve configuration, and a parametric study is performed to characterize how variations in key design parameters affect valve performance. Last some conclusions are given in Sec. VI.

II. Mathematical Model

The valve is partitioned into three interacting subsystems: the *actuator*, *gas expansion chamber*, and *surroundings*. As indicated in Fig. 2, the actuator and gas expansion chamber collectively contain all explosive and combustion product mass, whereas the surroundings contain the mass of all structural members including the piston and housing. The actuator interacts with the expansion chamber by mass and energy transport through a small port, and both interact thermally with the surroundings by convective and radiative heat transfer through their walls. It is assumed that all unreacted explosive mass is confined to the actuator, and gas product mass blowby past the piston is ignored. The expansion chamber also undergoes a work interaction with the surroundings due to volume changes associated with piston motion. Strain work interactions between the actuator and expansion chamber, and their surrounding walls, are ignored.

We first summarize in Sec. II.A the model equations for the actuator and expansion chamber subsystems. Because these equations are similar to those originally formulated by Gonthier et al. [14,15] for a pyrotechnically actuated pin puller model, the discussion is intentionally kept brief; the interested reader is referred to this cited work for a more comprehensive discussion. We then outline in Sec. II.B a technique to estimate the axial resistive force induced by piston–housing interactions as the piston is inserted into the valve bore.

A. Actuator and Expansion Chamber Model

Mass and thermal energy evolution equations can be expressed for the solid explosive and gaseous combustion products contained within the actuator and expansion chamber using mixture theory principles. The focus here is on gaseous combustion products because HMX produces very little condensed phase products when burned; nonetheless, the model may be easily extended to account for condensed phase products, which often result from pyrotechnic combustion, using the generic technique described in [14]. The combustion of HMX is taken to form gaseous product species (N_2,

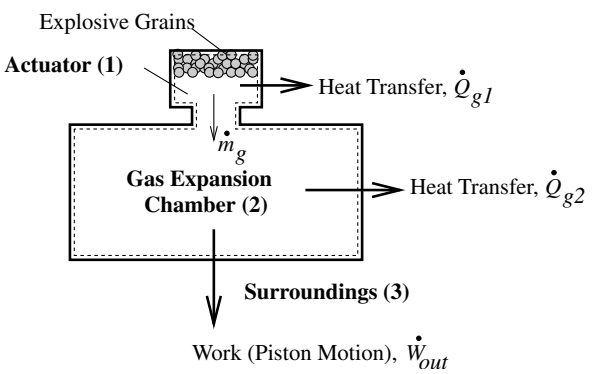

Fig. 2 Illustration of subsystem mass and energy interactions.

NO, CO_2, CO, H_2O, OH, H_2, H) indicated by equilibrium chemistry that imposed constant internal energy and actuator volume; the equilibrium calculations were performed using the commercial software package CHEMKIN. The product species specified by CHEMKIN are similar to those reported by Tarver [16] for finite-rate thermal decomposition of HMX. The stoichiometry for this global combustion process is given in the following expression:

$$\begin{aligned}C_4H_8N_8O_8(s) \rightarrow\ & 3.979N_2(g) + 2.971CO(g) + 2.908H_2O(g)\\ & + 1.005CO_2(g) + 0.999H_2(g) + 0.062OH(g) + 0.035H(g)\\ & + 0.002NO(g)\end{aligned}$$

Product species having mol concentrations less than 0.01 are ignored. The reactant and products are assumed to acoustically equilibrate much faster than the valve operation time resulting in a time-dependent, well-stirred reactor. The validity of this assumption can be established using representative values for the product gas specific heat ratio ($\gamma \approx 1.4$), ideal gas constant ($R \approx 300$ J/kg/K), and temperature ($T \approx 4000$ K), to estimate the time required for an acoustic disturbance to propagate across the expansion chamber ($l_c \approx 6$ mm): $t_c = l_c/\sqrt{\gamma RT} \approx 4.6$ μs. Because this time is not significantly smaller than the valve operation time (90 μs), temporal and spatial oscillations arising from compressible wave propagation may be important in describing the operation of these valves [17]. Nonetheless, the quasi-equilibrium assumption adopted here enables leading-order, spatially averaged predictions to be inexpensively obtained that are useful for preliminary design purposes.

Mass and thermal energy evolution equations for the explosive and gas products, coupled with an equation for piston motion, are given by the following ordinary differential equations (ODEs):

$$\frac{\mathrm{d}}{\mathrm{d}t}(\rho_s V_s) = -\rho_s A_b r_b \tag{1}$$

$$\frac{\mathrm{d}}{\mathrm{d}t}(\rho_{g_1} V_{g_1}) = \rho_s A_b r_b - \dot{m}_g \tag{2}$$

$$\frac{\mathrm{d}}{\mathrm{d}t}(\rho_s V_s e_s) = -\rho_s e_s A_b r_b \tag{3}$$

$$\frac{\mathrm{d}}{\mathrm{d}t}(\rho_{g_1} V_{g_1} e_{g_1}) = \rho_s e_s A_b r_b - h_{g_1}\dot{m}_g - \dot{Q}_{g_1} \tag{4}$$

$$\frac{\mathrm{d}}{\mathrm{d}t}(\rho_{g_2} V_{g_2}) = \dot{m}_g \tag{5}$$

$$\frac{\mathrm{d}}{\mathrm{d}t}(\rho_{g_2} V_{g_2} e_{g_2}) = h_{g_1}\dot{m}_g - \dot{Q}_{g_2} - \dot{W}_{\mathrm{out}} \tag{6}$$

$$m_p \frac{\mathrm{d}^2}{\mathrm{d}t^2}(z_p) = F_p - F_R \tag{7}$$

In these equations, subscripts "1" and "2" indicate quantities associated with the actuator and expansion chamber, respectively, and subscripts "s" and "g" indicate quantities associated with the solid explosive and gas phase products, respectively. The independent variable is time t. Dependent variables include the density ρ_{g_i} ($i = 1, 2$); the volumes V_s and V_{g_i}; the specific internal energies e_s and e_{g_i}; the specific enthalpy h_{g_1}; the piston position measured relative to the top of the expansion chamber z_p, as later indicated in Fig. 3; the explosive linear regression burning rate r_b; the area of the burning surface A_b; the product gas mass flow rate from the actuator to the expansion chamber $\dot{m}_g$; the heat transfer rates from the gas phase products to the surroundings $\dot{Q}_{g_i}$; the work rate done by product gases contained within the expansion chamber in moving the piston $\dot{W}_{\mathrm{out}}$; and the net gas pressure and resistive force acting on the piston F_p and F_R, respectively. Constant parameters contained in Eqs. (1–7) are the piston mass m_p and the unreacted solid explosive density ρ_s. Equations (1–4) govern the evolution of mass and internal energy for the solid explosive and gas phase products contained within the actuator, respectively, whereas Eqs. (5) and (6) govern the evolution of gas product mass and internal energy within the expansion chamber. Kinetic and potential energy are ignored. Summing Eqs. (1), (2), and (5) gives

$$\frac{\mathrm{d}}{\mathrm{d}t}(\rho_s V_s + \rho_{g_1} V_{g_1} + \rho_{g_2} V_{g_2}) = 0$$

consequently, the total explosive mass is conserved by this model. Likewise, summing Eqs. (3), (4), and (6) gives

$$\frac{\mathrm{d}}{\mathrm{d}t}(\rho_s V_s e_s + \rho_{g_1} V_{g_1} e_{g_1} + \rho_{g_2} V_{g_2} e_{g_2}) = -(\dot{Q}_{g_1} + \dot{Q}_{g_2}) - \dot{W}_{\mathrm{out}}$$

indicating that the total explosive and gas product energy changes only due to heat and work interactions with the surroundings. Further, it can be shown by multiplying Eq. (1) by e_s, and subtracting the result from Eq. (3), that the internal energy of the solid explosive remains constant for this analysis (i.e., $e_s = e_{s0}$) because heat transfer from the hot product gases to the explosive is ignored. Equation (7) is Newton's second law which governs the motion of the piston.

Constitutive relations needed to mathematically close Eqs. (1–7) include the following. Geometrical constraints require that $V_1 = V_s + V_{g_1}$, $V_2 = V_2(z_p) = V_{g_2}$, A_{w_1}, $A_{w_2} = A_{w_2}(z_p)$, and $A_p = A_p(z_p)$, where A_{w1} and A_{w2} are the surface areas of the actuator and expansion chamber through which heat transfer can occur with the surroundings, and A_p is the cross-sectional area of the top of the initially conical piston skirt. Geometrical variables that depend on piston location are indicated with a functional dependency on z_p; the specific relationships are straightforward and are eliminated for brevity. It is assumed that the solid explosive will fragment into N individually burning spherical grains immediately following ignition by the embedded hot wire. Expressions for the radius of each resulting spherical grain, their regression rate, and their total burning surface area are, respectively, given by

$$r = \left(\frac{3V_s}{4\pi N}\right)^{1/3}, \qquad r_b = -\frac{\mathrm{d}r}{\mathrm{d}t} = bP_{g_1}^n, \qquad A_b = (4\pi r^2 N) \tag{8}$$

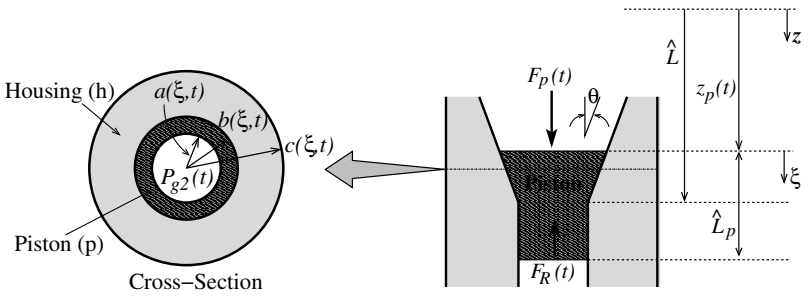

Fig. 3 Coordinate system used for establishing the geometric interference force that resists piston motion.

As commonly done in solid propellant combustion modeling, the burning rate is taken to be dependent on the gas pressure within the actuator P_{g_1}. Here, b and n are burning rate constants whose values are chosen based on published data, as discussed later. The behavior of the product gases is taken as ideal. Their thermal and caloric equations of state, and constant volume specific heats, are given by

$$P_{g_i} = \rho_{g_i} R T_{g_i}, \qquad e_{g_i} = \sum_{j=1}^{N_g} Y_g^j e_g^j, \qquad c_{vg_i} = \sum_{j=1}^{N_g} Y_g^j \frac{\mathrm{d}}{\mathrm{d}T_{g_i}}(e_g^j) \tag{9}$$

Because internal energy is a function of temperature only for ideal gases, the constant volume specific heat is obtained by differentiating the caloric equation of state with respect to temperature. Occurring in these expressions are the gas temperature T_{g_i}, the ideal gas constant for the gas phase products R (the ratio of the universal gas constant and the mean molecular weight of the product gases), and the constant mass fractions $Y_{g_i}^j$ of the N_g product species. The notation superscript "j" is used to label quantities associated with individual chemical species. The thermodynamic properties of each species are calculated using the CHEMKIN subroutine library and database. Expressions for the specific enthalpy and constant pressure specific heat for the product gases contained within the actuator are given by

$$h_{g_1} = \sum_{j=1}^{N_g} Y_g^j h_g^j, \qquad c_{pg_1} = \sum_{j=1}^{N_g} Y_g^j \frac{\mathrm{d}}{\mathrm{d}T_{g_1}}(h_g^j) \tag{10}$$

Again, for ideal gases, the constant pressure specific heat is obtained by differentiating the enthalpy with respect to temperature.

Heat loss from the high temperature product gases to the cooler surroundings is assumed to occur by both convective and radiative heat transfer. The heat loss rates are given by

$$\begin{aligned} \dot{Q}_{g_1} &= hA_{w_1}(T_{g_1} - T_w) + \sigma A_{w_1}\left(\epsilon T_{g_1}^4 - \alpha T_w^4\right) \\ \dot{Q}_{g_2} &= hA_{w_2}(T_{g_2} - T_w) + \sigma A_{w_2}\left(\epsilon T_{g_2}^4 - \alpha T_w^4\right) \end{aligned} \tag{11}$$

where h is a constant convective heat transfer coefficient, T_w is the temperature of the surrounding walls, σ is the Stefan–Boltzmann constant, α is the absorptivity of the walls, and ϵ is the net emissivity of the product gases. The pressure–volume work done by the gas contained within the expansion chamber in moving the piston is given by

$$\dot{W}_{\text{out}} = P_{g_2} \frac{\mathrm{d}V_2}{\mathrm{d}t} \tag{12}$$

and the net axial pressure force acting on the piston is given by

$$F_p = P_{g_2} A_p \tag{13}$$

All product mass is contained within the actuator until its pressure exceeds a critical value P_{crit} (55 MPa) that causes the burst disc to rupture. Once the disc is ruptured, the flow rate of gas product mass from the actuator to the expansion chamber is governed by the quasi-steady compressible flow relation

$$\dot{m}_g = \begin{cases} \rho_{g_1} A_e \sqrt{\gamma R T_{g_1}} \sqrt{\frac{2}{\gamma-1}\left(\frac{P_{g1}}{P_{g_2}}\right)^{-\frac{\gamma+1}{\gamma}}\left[\left(\frac{P_{g1}}{P_{g_2}}\right)^{\frac{\gamma-1}{\gamma}} - 1\right]} & \text{if } \left(\frac{P_{g1}}{P_{g_2}}\right) < \left(\frac{\gamma+1}{2}\right)^{\frac{\gamma}{\gamma-1}} \\ \rho_{g_1} A_e \sqrt{\gamma R T_{g_1}} \left(\frac{2}{\gamma+1}\right)^{\frac{\gamma+1}{2(\gamma-1)}} & \text{if } \left(\frac{P_{g1}}{P_{g_2}}\right) \geq \left(\frac{\gamma+1}{2}\right)^{\frac{\gamma}{\gamma-1}} \end{cases} \tag{14}$$

Occurring in this expression is the specific heat ratio for the product gases contained within the actuator $\gamma\ (=c_{pg_1}/c_{vg_1})$. This expression accounts for mass choking at elevated actuator/expansion chamber pressure ratios.

An important, yet undefined, variable in Eq. (7) is the force F_R that resists piston motion due to geometrical interference between the piston and housing. Properly estimating the magnitude of this force and its dependence on both piston and housing material properties and geometry, and on gas pressure within the expansion chamber, is key to obtaining a predictive model. Fundamental design decisions often focus on component material selection and geometry that can significantly affect the resistive force. The technique used to estimate this force is outlined in the following section.

Equations (1–14) can be reduced by mathematical operations to a final autonomous system of first order ODE's that can be numerically solved to predict valve performance. To this end, it is necessary to define a new variable $\dot{V}_2$ representing the time derivative of the gas expansion chamber volume:

$$\dot{V}_2 \equiv \frac{\mathrm{d}V_2}{\mathrm{d}t} \tag{15}$$

The final system consists of six first order ODE's of the form

$$\frac{\mathrm{d}\mathbf{u}}{\mathrm{d}t} = \mathbf{f}(\mathbf{u}) \tag{16}$$

where $\mathbf{u} = (V_2, V_s, \rho_{g_1}, T_{g_1}, T_{g_2}, \dot{V}_2)^T$ is a vector of dependent primary variables and $\mathbf{f}$ is a nonlinear vector function. All remaining variables can be expressed in terms of these six primary variables. The operations used to express the model equations in this reduced form are omitted for brevity as they are discussed in detail by Gonthier et al. [14,15]. Initial conditions for these equations are

$$\begin{aligned} V_2(0) &= V_{20} \qquad V_s(0) = V_{s0} \qquad \rho_{g_1}(0) = \rho_{g1_0} \\ T_{g_1}(0) &= T_0 \qquad T_{g_2}(0) = T_0 \qquad \dot{V}_2(0) = 0 \end{aligned} \tag{17}$$

B. Piston–Housing Deformation Model

A technique is described in this section for predicting time-dependent resistance to piston motion due to interference between the piston skirt and housing as the piston is pushed into the bore by the high pressure gas contained within the expansion chamber. A similar technique was used by Jones et al. [11,12] to model piston motion within an explosively actuated valve, though differences exist between our descriptions which are highlighted later. A premium is placed on tractability; thus, simple analytical solutions for material mechanics that do not require the application of elaborate finite-element modeling techniques are used. The use of analytical solutions facilitates extensive parametric studies with minimal computational times due to their relative simplicity. Because thermal energy evolution within the surrounding structure is not accounted for, emphasis is placed on estimating mechanical stresses induced within the piston and housing by geometrical interference and internal gas pressure only. Thermal stresses within this structure, although potentially significant at elevated temperature, would

require a more detailed thermomechanics model. The deformation model formulated in this section shall be referred to as the simple model in that it is analytically based.

It is assumed that the piston skirt initially lies entirely within the tapered region of the expansion chamber, as indicated in Fig. 1a, referred to as the skirt region. Immediately following actuation, part of the piston skirt is pushed into the bore, while part remains within the skirt region, as indicated in Fig. 3. Thus, time-dependent resistance to piston motion is generally due to interference experienced within both the skirt and bore regions of the valve:

$$F_R(t) = F_{\text{skirt}}(t) + F_{\text{bore}}(t) \tag{18}$$

Functional dependencies are included in the discussion that follows so that the coupling between spatial and temporal quantities is apparent. Initially, $F_{\text{skirt}} = F_{\text{bore}} = 0$, and $F_{\text{skirt}} \to 0$ as the entire piston is pushed into the bore. The geometrical interference and gas pressure within the hollow piston increase the magnitude of the compressive radial stress at the axisymmetric piston–housing interface, that is, $\sigma_r = -\tilde{P}$. This radial interface stress is assumed to locally induce a tangential frictional stress $\tilde{\tau} = \mu\tilde{P}$, where μ is a constant friction coefficient. As discussed in the following section, it is necessary to use different values of μ for the skirt and bore regions of the valve to implicitly account for the complex mechanics induced by the corner connecting these regions. Because the interference varies with both position along the piston axis and time, then $\tilde{P} = \tilde{P}(\xi, t)$ and $\tilde{\tau} = \tilde{\tau}(\xi, t)$, where ξ is the position measured relative to the upper piston surface, as indicated in Fig. 3. Because of geometric variations in the piston and housing, the inner, interface, and outer radii for a cross section of the piston–housing structure are locally given by $a(\xi, t)$, $b(\xi, t)$, and $c(\xi, t)$, respectively; these radii are indicated in the figure. Using the coordinates defined in the figure and the geometry illustrated in Fig. 4, where the valve attached axial coordinate z is measured relative to the top of the expansion chamber, the following expressions for the time-dependent resistive force components in the direction of piston motion result:

$$\begin{aligned} F_{\text{skirt}}(t) &= (\mu_s \cos\theta + \sin\theta) \int_{A_{\text{skirt}}} \tilde{P}(\xi, t)\, \mathrm{d}A \\ F_{\text{bore}}(t) &= \mu_b \int_{A_{\text{bore}}} \tilde{P}(\xi, t)\, \mathrm{d}A \end{aligned} \tag{19}$$

where θ is the inclination of the skirt with respect to the vertical. The integration indicated here is performed over the interfacial surface area of the skirt and bore regions of the piston. In this work, the skirt region has the shape of a partial cone and the bore region has the shape of a cylinder; thus, the area integrals in Eq. (19) can be reduced to 1-D integrals in terms of the axial piston coordinate ζ:

$$\begin{aligned} F_{\text{skirt}}(t) &= (\mu \cos\theta + \sin\theta) \int_0^{\hat{L}-z_p(t)} \tilde{P}(\xi, t) g(\xi, t)\, \mathrm{d}\xi \\ F_{\text{bore}}(t) &= 2\pi\mu R_b \int_{\hat{L}-z_p(t)}^{\hat{L}_p} \tilde{P}(\xi, t)\, \mathrm{d}\xi \end{aligned} \tag{20}$$

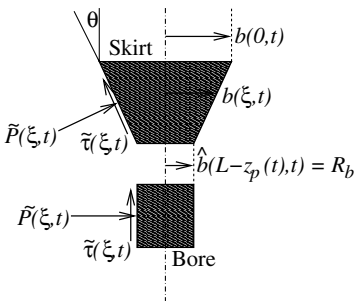

Fig. 4 Schematic illustrating the separation of the piston into skirt and bore components for computing their contributions to the total resistive force.

where

$$g(\xi, t) = \pi\sqrt{[b(0,t) - b(\xi,t)]^2 + \xi^2} \times \left\{ \frac{\partial b}{\partial \xi} + \frac{[b(0,t) + b(\xi,t)](\xi - [b(0,t) - b(\xi,t)]\frac{\partial b}{\partial \xi})}{[b(0,t) - b(\xi,t)]^2 + \xi^2} \right\}$$

and

$$b(\xi, t) = \left[\frac{R_b - b(0,t)}{\hat{L} - z_p(t)}\right]\xi + b(0,t)$$

Here $b(0, t)$ is the interface radius at the top of the piston, R_b is the constant bore radius, and $b(\xi, t)$ is the variable interface radius between these limits. Both the piston and housing are assumed to experience only small deformations; thus variations in piston length associated with its deformation are ignored. This assumption is reasonable for the nitrogen cartridge valves studied in this work because $\theta \ll 1$.

To complete the model, it is necessary to estimate $\tilde{P}(\xi, t)$ so that the total resistive force can be computed from Eq. (20) and the result coupled to the equation of motion for the piston given by Eq. (7). The local interface stress is estimated based on a 2-D plane strain analysis which assumes that the stress state within the piston skirt and housing rapidly equilibrates during piston motion. To determine the validity of this assumption, it is reasonable to consider the time required for an elastic wave to travel through the housing thickness. The characteristic time for an elastic wave to traverse a housing of local thickness $\mathrm{d_c} = 14$ mm is $t_c = 2\mathrm{d_c}\sqrt{\rho/E} \approx 3$ μs (for $E = 214$ GPa and $\rho = 7800$ kg/m^3 which are representative of steel). Because t_c is not significantly less than t_{op}, where $t_{\text{op}} \approx 90$ μs is the characteristic valve operation time, transient effects may be important in accurately describing the mechanical behavior of the valve. However the equilibrium assumption is used for its simplicity and to capture leading-order effects.

The following analysis is largely based on cylindrical pressure vessel theory. Shear stresses ($\tau_{r\theta} = \tau_{rz} = \tau_{\theta z} = 0$) are ignored and it is assumed that $\hat{\hat{\boldsymbol{\sigma}}} = \hat{\hat{\boldsymbol{\sigma}}}(r; \xi, t)$, where there exists a parametric dependence on ξ and t; consequently, the stress state is locally defined by the radial stress σ_r, the hoop stress σ_θ, and the axial stress σ_z, which are the principal values of $\hat{\hat{\boldsymbol{\sigma}}}$. Based on these assumptions, the equilibrium form of the angular and axial momentum field equations for the composite piston and housing structure are identically satisfied for fixed ξ and t, and the radial momentum equation reduces to

$$\frac{\mathrm{d}\sigma_r}{\mathrm{d}r} + \frac{\sigma_r - \sigma_\theta}{r} = 0 \tag{21}$$

We seek analytical elastic–plastic solutions to the boundary value problem defined by Eq. (21) for the generic cross-sectional member illustrated in Fig. 3 subject to the surface stresses $\sigma_r(a; \xi, t) = -P_{g_2}(t)$ and $\sigma_r(c; \xi, t) = 0$ and a geometric interference between the piston skirt and housing given by $\delta(\xi, t)$. It is essential to account for plastic deformation as it significantly affects interface stress and enables hardening to be described. It is shown in Sec. III.B that significant plastic deformation occurs within the piston. The strategy is to first obtain a general solution to Eq. (21) for a single annular disc undergoing elastic–plastic deformation that can be used to separately describe the displacement and stress fields within the piston skirt and housing. A particular coupled solution for the composite member is then obtained by imposing $\sigma_r(a; \xi, t) = -P_{g_2}(t)$ at the internal piston surface, $\sigma_r(c; \xi, t) = 0$ at the external housing surface, and $\sigma_r(b; \xi, t) = -\tilde{P}$ at the piston–housing interface. Geometrical interference between the piston skirt and housing requires that $u_h(b; \xi, t) - u_p(b; \xi, t) = \delta(\xi, t)$, where u_p and u_h are radial displacements for the piston skirt and housing, respectively. In the following paragraphs, general solutions of this problem are summarized; detailed derivations of these solutions are not provided as they are published elsewhere [18].

Equation (21) can be combined with the stress–strain relations for a Hookean elastic solid, and the strain-displacement relations $\epsilon_r = \mathrm{d}u/\mathrm{d}r$ and $\epsilon_\theta = u/r$, where u is the radial displacement field, to obtain the following linear, homogeneous ODE:

$$r^2\frac{\mathrm{d}^2u}{\mathrm{d}r^2} + r\frac{\mathrm{d}u}{\mathrm{d}r} - u = 0$$

The general solution of this equation is given by

$$u(r;\xi,t) = \frac{\mathcal{A}(\xi,t)}{r} + \mathcal{B}(\xi,t)r \tag{22}$$

where $\mathcal{A}$ and $\mathcal{B}$ are integration constants that are parameterized by ξ and t. The following stress fields result from this displacement field:

$$\sigma_r(r;\xi,t) = \frac{E}{1+\nu}\left[-\frac{\mathcal{A}(\xi,t)}{r^2} + \frac{\mathcal{B}(\xi,t)}{1-2\nu}\right] \tag{23}$$

$$\sigma_\theta(r;\xi,t) = \frac{E}{1+\nu}\left[\frac{\mathcal{A}(\xi,t)}{r^2} + \frac{\mathcal{B}(\xi,t)}{1-2\nu}\right] \tag{24}$$

$$\sigma_z(\xi,t) = \frac{2\nu E\mathcal{B}(\xi,t)}{(1+\nu)(1-2\nu)} \tag{25}$$

where E and ν are Young's modulus and Poisson's ratio, respectively. It is noted that σ_z is constant for fixed ξ and t in this case.

A general plastic solution to Eq. (21) is obtained based on Tresca's yield criterion with linear strain hardening. To this end, total strain is partitioned into elastic and plastic components. The yield criterion is given by $\sigma_{\mathrm{I}} - \sigma_{\mathrm{III}} = \sigma_y(|\epsilon_r^p|)$, where

$$\sigma_y\left(\left|\epsilon_r^p\right|\right) = \sigma_0\left(1 + \eta\left|\epsilon_r^p\right|\right)$$

Here, σ_{I} and σ_{III} are the maximum and minimum principal stresses, and σ_y is the material yield strength in simple tension that increases with the magnitude of the plastic radial strain ϵ_r^p. The linear hardening parameter is η, and the reference yield stress corresponding to $\eta = 0$ is σ_0. The magnitude of the plastic radial strain is directly proportional to the equivalent plastic strain, that is $\epsilon_r^p \propto \epsilon_{\mathrm{EQ}}$, because compatibility of the plastic flow relations associated with the yield criterion requires that $\epsilon_r^p = -\epsilon_\theta^p$. It is important to note that the ordering of principal stresses is important for properly establishing yielding and subsequent plastic flow. Two cases are considered: $\sigma_r > \sigma_z > \sigma_\theta$ and $\sigma_\theta > \sigma_z > \sigma_r$.

Case 1: $\sigma_r > \sigma_z > \sigma_\theta$. For this case, the equilibrium condition of Eq. (21), together with the yield criterion, the stress-total strain relations, and the strain-displacement relations, results in the following linear, inhomogeneous ODE for the radial displacement field:

$$r^2\frac{\mathrm{d}^2u}{\mathrm{d}r^2} + r\frac{\mathrm{d}u}{\mathrm{d}r} - u = -\frac{2\sigma_0(1+\nu)(1-2\nu)}{E[1+H(1-\nu^2)]}r$$

where H is a dimensionless hardening parameter defined by $H \equiv \eta\sigma_0/E$; its general solution is given by

$$u(r;\xi,t) = \frac{\mathcal{A}(\xi,t)}{r} + \mathcal{B}(\xi,t)r - \frac{\sigma_0(1+\nu)(1-2\nu)(2\,\ell_n\, r - 1)r}{2[1+H(1-\nu^2)]} \tag{26}$$

where, again, $\mathcal{A}$ and $\mathcal{B}$ are integration constants. The corresponding stress fields are given by

$$\sigma_r(r;\xi,t) = -\frac{EH\mathcal{A}(\xi,t)}{[2+H(1+\nu)]r^2} + \frac{E\mathcal{B}(\xi,t)}{(1+\nu)(1-2\nu)} - \frac{\sigma_0(2\,\ell_n\, r - 1)}{2[1+H(1-\nu^2)]} \tag{27}$$

$$\sigma_\theta(r;\xi,t) = \frac{EH\mathcal{A}(\xi,t)}{[2+H(1+\nu)]r^2} + \frac{E\mathcal{B}(\xi,t)}{(1+\nu)(1-2\nu)} - \frac{\sigma_0(2\,\ell_n\, r + 1)}{2[1+H(1-\nu^2)]} \tag{28}$$

$$\sigma_z(r;\xi,t) = \frac{2E\nu\mathcal{B}(\xi,t)}{(1+\nu)(1-2\nu)} - \frac{2\sigma_0\nu\,\ell_n\, r}{1+H(1-\nu^2)} \tag{29}$$

In this instance, the axial stress varies with radial position unlike that for purely elastic deformation.

Case 2: $\sigma_\theta > \sigma_z > \sigma_r$. For this case, the radial displacement field is governed by the ODE

$$r^2\frac{\mathrm{d}^2u}{\mathrm{d}r^2} + r\frac{\mathrm{d}u}{\mathrm{d}r} - u = \frac{2\sigma_0(1+\nu)(1-2\nu)}{E[1+H(1-\nu^2)]}r$$

whose general solution is given by

$$u(r;\xi,t) = \frac{\mathcal{A}(\xi,t)}{r} + \mathcal{B}(\xi,t)r + \frac{\sigma_0(1+\nu)(1-2\nu)(2\,\ell_n\, r - 1)r}{2[1+H(1-\nu^2)]} \tag{30}$$

The corresponding stress fields are

$$\sigma_r(r;\xi,t) = -\frac{EH\mathcal{A}(\xi,t)}{[2+H(1+\nu)]r^2} + \frac{E\mathcal{B}(\xi,t)}{(1+\nu)(1-2\nu)} + \frac{\sigma_0(2\,\ell_n\, r - 1)}{2[1+H(1-\nu^2)]} \tag{31}$$

$$\sigma_\theta(r;\xi,t) = \frac{EH\mathcal{A}(\xi,t)}{[2+H(1+\nu)]r^2} + \frac{E\mathcal{B}(\xi,t)}{(1+\nu)(1-2\nu)} + \frac{\sigma_0(2\,\ell_n\, r + 1)}{2[1+H(1-\nu^2)]} \tag{32}$$

$$\sigma_z(r;\xi,t) = \frac{2E\nu\mathcal{B}(\xi,t)}{(1+\nu)(1-2\nu)} + \frac{2\sigma_0\nu\,\ell_n\, r}{1+H(1-\nu^2)} \tag{33}$$

Depending on the material properties of the piston and housing, a given loading scenario (i.e., geometric interference δ and gas pressure P_{g_2}) will involve an initially elastic response followed by plastic deformation with strain hardening within the piston and/or housing. It can be easily shown that plastic deformation of the piston and housing initiates at their respective inner surfaces and subsequently flows radially outward until their annuli are fully plastic. Because of the intense gas pressure generated by HMX combustion, and the short valve operation time, it is anticipated that transition to full plasticity will rapidly occur for reasonably thin members such as the piston skirt. To simplify the analysis, the plastic flow rate in the piston is assumed fast compared with the valve operation time, and contained plasticity is ignored; as such, the piston instantaneously becomes fully plastic at a cross-section following the onset of yielding. The housing is generally much thicker than the piston, therefore it is more appropriate to model it as undergoing contained rather than uncontained plasticity. The plastic radius $\mathrm{d}(\xi,t)$ initially forms at the housing inner radius, and then propagates outward to a location between its inner and outer radii ($b < d < c$).

Equations (22) and (33) are separately applicable to both the piston and housing. Assuming uncontained plasticity following the onset of yielding in the piston and contained plasticity in the housing, values for the integration constants $\mathcal{A}_{p\beta}$, $\mathcal{B}_{p\beta}$, $\mathcal{A}_{h\kappa}$, and $\mathcal{B}_{h\kappa}$, $\mathcal{A}_{h\beta}$, and $\mathcal{B}_{h\beta}$, and plastic radius d, are determined, for fixed ξ and t, by simultaneously solving the following coupled nonlinear equations that result from imposing the boundary conditions:

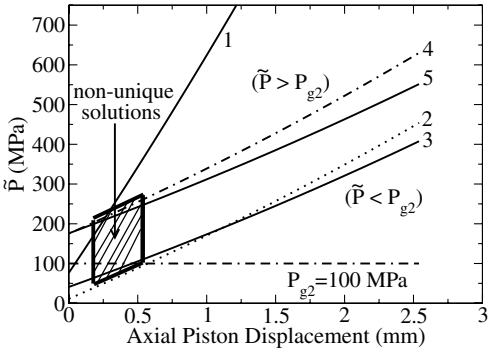

Fig. 5 Graphical summary of steady solutions for the variation in interface stress near the top of the piston skirt with piston displacement.

$$\sigma_{r,p\beta}(a;\xi,t) = -P_{g2}(t) \qquad \sigma_{r,p\beta}(b;\xi,t) = \sigma_{r,h\beta}(b;\xi,t)$$
$$\sigma_{r,h\kappa}(\mathrm{d};\xi,t) = \sigma_{r,h\beta}(\mathrm{d};\xi,t) \qquad \sigma_{r,h\kappa}(c;\xi,t) = 0$$
$$u_{h\beta}(b;\xi,t) - u_{p\beta}(b;\xi,t) = \delta(\xi,t) \qquad u_{h\kappa}(\mathrm{d};\xi,t) = u_{h\beta}(\mathrm{d};\xi,t)$$
$$\sigma_{\theta,h\kappa}(\mathrm{d};\xi,t) = \sigma_{\theta,h\beta}(\mathrm{d};\xi,t) \tag{34}$$

This reduced set of nonlinear equations is iteratively solved using a Newton–Raphson numerical technique. Here, subscripts p and h denote quantities associated with the piston and housing, and subscripts κ and β refer to the plastic and elastic regions of the housing, respectively. It is important to note that appropriate expressions for u [Eqs. (22) and (26), or (30)] and σ_r [Eqs. (23) and (27), or (31)] used with these boundary conditions depends on whether the piston and housing are elastic or plastic and, if plastic, whether σ_r is less or greater than σ_θ.

As mentioned, plastic solutions for the stress and displacement fields within both the piston and housing depend on the ordering of the principal stresses. This ordering depends on the sign of the hoop stress in each member; that is, whether the member yields due to a large internal pressure (positive hoop stress) or external pressure (negative hoop stress). The ordering of principal stresses in the housing is easily determined because it will always yield due to a sufficiently large interface pressure in the absence of applied external pressure. The proper ordering of principal stresses in the piston experiencing both large internal and interface pressure, however, is not known a priori; as such, an assumption must be made about the ordering during the solution procedure that can be later verified based on plausibility arguments.

Figure 5 graphically summarizes different steady solutions for interface stress $\tilde{P}$ near the top of the piston skirt as a function of axial piston displacement. These results were obtained for a piston skirt thickness of 0.6429 mm, length of 2.54 mm, and inclination angle of 9 deg with respect to the valve axis, and inner and outer housing radii of 5.969 and 12.7 mm, respectively; these values completely determine the piston skirt–housing geometry for the deformation model and are used throughout our analysis for the baseline valve configuration. Material properties for the piston skirt and housing are listed later in Table 3. Solution 1 corresponds to a purely elastic piston and housing. Solutions 2 and 3 correspond to $\tilde{P} < P_{g2} =$ 100 MPa initially, where solution 2 is for an elastic housing and plastic piston, and solution 3 is for a plastic piston and plastic housing. Solutions 4 and 5 correspond to $\tilde{P} > P_{g2} = 100$ MPa initially, where solution 4 is for an elastic housing and plastic piston, and solution 5 is for a plastic piston and plastic housing. A small range of axial displacement is predicted where the solution for $\tilde{P}$ is nonunique for this given value of P_{g2}, indicated by the highlighted region in the figure; here, nonunique means that solutions 2–5 each satisfy their assumptions regarding the ordering of principal stresses, that is $\tilde{P} > P_{g2}$ or $\tilde{P} < P_{g2}$. Because solutions 2 and 3 only satisfy the proper ordering of principal stresses within the highlighted region, whereas solutions 3 and 4 also satisfy the ordering outside of this region, solutions 3 and 4 are chosen as proper solutions. To avoid choosing improper solutions in the implementation of the deformation model, an algorithmic logic is used to maintain continuity in $\tilde{P}$ for a given cross section.

Lastly the assumption of plane strain provides consistency between the elastic and plastic solutions, unlike the work of Jones et al. [11,12], which assumes plane stress for the elastic response and plane strain for the plastic response. It is shown in Sec. III.B that axial stresses are important for describing the stress field within the piston so that the plain strain assumption might appear more appropriate than plane stress. Nonetheless, our predictions indicate that little difference exists between the integrated plane strain and plane stress response of the system.

III. Inert, Quasi-Static Valve Operation

A technique was outlined in the previous section to estimate the axial resistive force acting on the piston during its insertion into the valve bore. In this section, we give results from inert, quasi-static compression tests that characterize both the variation in applied axial force with piston displacement and the overall energy requirements of the valve. We then show that the simple deformation model can describe key features of these tests if separate friction coefficient values are used for the skirt and bore regions of the valve. A quasi-static FEA prediction is given for the variation in integrated axial resistance force with piston displacement, and the prediction is compared with that of the simple model and the compression tests data. Importantly the FEA provides useful insight into the deformation and stress fields within the piston and housing, and enables the validity of certain simple model assumptions to be established.

A. Compression Tests

Inert, quasi-static compression tests were performed using an MTS™ Systems testing machine having a 88,960 N (20,000 lbf) load cell. For these tests, the valve was firmly attached to a support frame and placed onto the lower fixed platen of the MTS machine. A specially designed cylindrical ram made of hardened tool steel was vertically inserted into the valve through the actuator port until it firmly rested on top of the piston. The upper platen of the MTS machine was carefully lowered until it was flush with the top surface of the ram; it was then lowered at a constant extension rate of 2.54 mm/ min, until the piston contacted the stops, while the applied axial force and displacement were simultaneously recorded. Six tests were performed, though two of these tests were prematurely terminated due to a support frame malfunction. It is important to note that the MTS tests differ from explosive actuation in that both strain rate effects and hydrodynamic pressure loading are absent. During explosive actuation, the piston is hydrodynamically loaded, whereas during the MTS tests the valve is loaded with a concentrated force at the location where the ram contacts the piston. Though the MTS tests do not replicate explosive actuation, they were performed for both their simplicity and ability to provide quantitative data on the energy requirements of the valve.

Figure 6a gives the measured applied force (equals resistive force for quasi-static loading) for six MTS tests performed on new nitrogen cartridge valves. The data have been adjusted for the small measured compliance in the valve support plates. There is initially no resistive force due to zero interference between the piston and housing. As the ram displaces the piston, interference develops which increases the resistive force to a maximum value of approximately 12 kN before fully inserting the piston into the bore. The resistive force subsequently decreases as the piston is further displaced. The small kink that is visible near the approximate location where the skirt is first completely displaced into the bore ($\approx$2.54 mm), and during initial loading ($\approx$5 kN), is attributable to reversible deformation of the support frame. There is then a gradual increase in resistive force as the piston contacts the metal diaphragm that seals the nitrogen gas. A gradual bulging of the diaphragm is measured before it is punctured as the process takes place over a piston displacement of approximately 0.75 mm. The resistive force then remains relatively

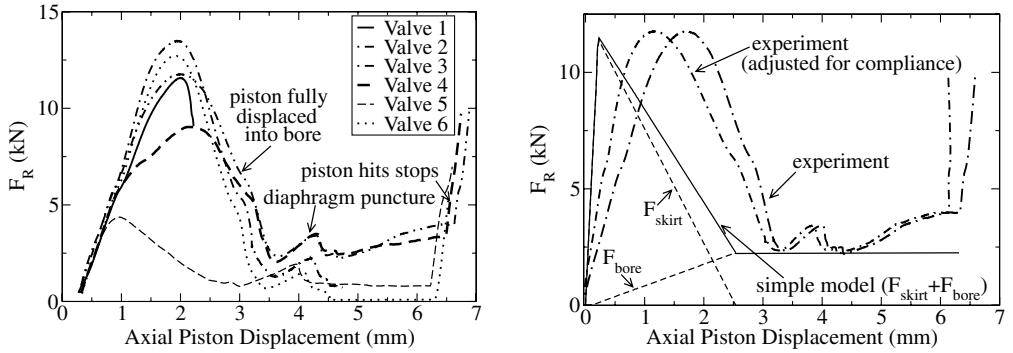

Fig. 6 a) Quasi-statically measured force-displacement curves for the piston within a nitrogen cartridge valve. b) Comparison of quasi-static data with simple deformation model predictions.

low and constant after the piston is further displaced within the bore until the stops are reached, which causes an abrupt increase in force. The large difference in measured resistive force occurring within the skirt and bore regions of the valve is consistent with large deformation extrusion processes [19]. The sharp corner connecting the skirt and bore regions induces large bending stresses within the piston skirt which effectively reduces its geometric interference when traversing the corner and entering the bore. This observation suggests that different friction coefficient values may be used for the skirt and bore regions to implicitly account for the complex structural mechanics induced by the corner, as demonstrated below. These qualitative trends were observed for all valves tested, but there were quantitative differences in several of the measured force-displacement profiles. The reason for these differences is not apparent, though slight differences in valve geometry and eccentric loading conditions are possible causes.

Table 1 lists the work contributions required to insert the piston skirt into the bore, to push the fully inserted piston over the bore length, and to puncture the diaphragm, as a percentage of the total work required to function the valve. Only data from valves 3–6 are shown due to incomplete data sets obtained for valves 1 and 2. The work requirements were calculated by numerically integrating the experimental force-displacement data. The work required for piston skirt insertion was computed by integrating the data from the initial piston location to the location where the skirt was first entirely displaced into the bore. The work required for bore travel was computed by integrating the data from the location where the piston was first entirely inserted into the bore to the location where it first contacted the stops. The work required to puncture the diaphragm was computed by integrating the data from the location where the resistive force starts to rise due to piston–diaphragm contact to the location where the force levels off after puncture. It is apparent that the work needed to insert the piston skirt is the largest fraction of total valve work. Diaphragm puncture plays a minimal role in the valve work requirements, accounting for less than 16% of the work requirements in any of the valves. The average work required to puncture the diaphragm was approximately 2.1 J, corresponding to an equivalent piston velocity of 23 m/s based on kinetic energy.

Figure 6b compares the measured force profile for valve 3 with a prediction given by the simple model. The predicted net axial resistive force is shown, as are the contributions to this force from the skirt and bore regions of the valve. A friction coefficient value of

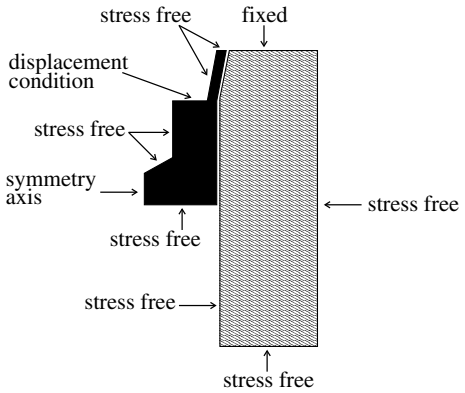

Fig. 7 Axisymmetric geometry and boundary conditions used for the FEA simulations.

$\mu_s = 0.9$ was used for the skirt region, and a value of $\mu_b = 0.2$ was used for the bore region. The value of μ_s was chosen to approximately match the peak measured resistive force, whereas the value of μ_b was chosen to approximately match the measured residual resistive force occurring once the piston was fully displaced into the bore. The measured and predicted results qualitatively differ in that the measured profile is broader than the prediction. This difference may be a consequence of deviations in piston material properties and the existence of large bending stresses within the piston that are not accounted for by the simple model. In fact, numerical experiments using the simple model indicate that the inclusion of linear strain hardening for the piston better represents the measured result [20], though material testing indicates that the piston more closely behaves as perfectly plastic.

B. Finite-Element Analysis

Results of a quasi-static FEA are now given which characterize how deformation and stress fields within the piston and housing vary with piston displacement, and how these fields affect the integrated axial resistive force. The commercial package ANSYS was used to perform the simulations for three values of friction coefficient: $\mu = 0.0, 0.1$, and 0.3. Computer memory limitations constrained the

Table 1 Quasi-static work requirements of the nitrogen cartridge valve

		Percentage of total work		
Valve	Total work, J	Skirt insertion	Bore travel	Puncture
	(24.14 ± 10.6 J)	(61.6 ± 12.9%)	(38.4 ± 12.9%)	(9.6 ± 4.8%)
3	34.56	54.07	45.93	7.79
4	28.76	51.00	49.00	10.50
5	9.82	61.57	38.43	15.81
6	23.45	79.76	20.24	4.33

Table 2 Material property data used in the FEA simulations

	Piston (SS 17-4PH)		Housing (304L)	
Parameter	Value	Unit	Value	Unit
Elastic modulus	200.0	GPa	214.0	GPa
Yield stress	758.0	MPa	275.0	MPa
Plastic modulus	0.0	GPa	74.9	GPa
Poisson's ratio	0.3	——	0.3	——

resolution needed to perform simulations with higher friction coefficient values. Figure 7 shows the axisymmetric geometry and boundary conditions imposed for the simulations. To closely replicate the MTS tests, a displacement boundary condition was applied to the ram contact surface, and a zero displacement boundary condition was applied to the top of the housing mimicking the screws that held the valve in place during the tests. The valve centerline is the axis of symmetry. All remaining surfaces are initially stress free. For each simulation, a displacement was imposed, and the corresponding steady solution was computed. Data were extracted and analyzed using ANSYS postprocessing. A sufficient number of displacements were imposed so that the entire piston insertion process could be analyzed. The piston was modeled as elastic-perfectly plastic, and the housing was modeled as elastic–plastic with linear strain hardening; Table 2 lists values for the material properties used in the simulations. These values were chosen to approximately match tensile test data for both the piston and housing. A penalty based method was used to model contact between the piston and housing.

Figure 8a compares predictions for the axial resistive force given by both the simple model and the FEA with the measured result for valve 3. The FEA predictions, which are integrated forces along the piston–housing interface, are qualitatively similar to the simple model prediction in that the force linearly increases to a maximum value before linearly decreasing, and approaches a nearly constant value as the piston is completely displaced into the bore. The stiffness of the initial force-displacement response increases with friction coefficient. There is reasonable qualitative agreement between the simple model and FEA predictions, including the approximate displacement for maximum force. It is anticipated that larger friction coefficient values used in the FEA would result in larger forces that would better agree with both the simple model prediction and the MTS tests. Again, the FEA prediction is not as broad as the measured force-displacement profile. In the remainder of this section, FEA predictions are given for a friction coefficient of $\mu = 0.3$ because it most closely represents the measured data.

To assess the validity of the simple deformation model, it is instructive to compare stress distributions along the piston–housing interface predicted by the simple model and the FEA, as shown in Fig. 8b for 25% piston insertion; similar results exist for other insertion distances. For this displacement, part of the piston skirt is located in both the skirt and bore regions of the valve. The ordering of the FEA predicted interface stresses is consistent with that given by the simple model; that is, $\sigma_r > \sigma_z > \sigma_\theta$. There is little predicted change in stress state along much of the interface due to both a perfectly plastic piston and a small skirt deflection angle ($\theta = 9$ deg). It is noted that the FEA predicted stress magnitudes significantly increase in the immediate vicinity of the housing corner suggesting that large bending stresses are induced within the piston. The simple model does not predict such stresses, though their integrated effect may not be large as suggested by qualitative agreement between the simple model and FEA predictions for the net resistive force. The development of more rigorous constitutive theories that better account for these bending stresses is an ongoing topic of our research. It has been additionally verified by equivalent stress contour plots that the assumption of contained plasticity within the housing, and uncontained plasticity within the piston, are entirely appropriate during piston insertion.

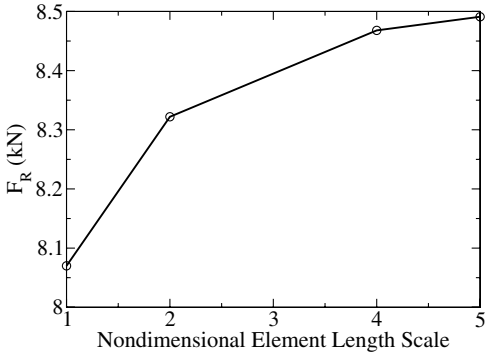

Fig. 9 Numerical convergence results for the FEA simulations.

Figure 9 summarizes numerical convergence results for the FEA. Shown in the figure is the predicted variation in net resistive force with a nondimensional characteristic finite-element size for a piston insertion depth of 12.5%. The nondimensional element size is defined as $l^* \equiv l_c/l$, where l_c and l are dimensional characteristic element sizes corresponding to the coarsest and finer meshes, respectively. The characteristic sizes were chosen as the average of all elements within the computational domain for a given simulation. Because of computer memory constraints, more refined computational grids ($l^* > 5$) could not be analyzed. Nonetheless, the results of Fig. 9 suggest a second-order convergence rate. All simulations performed in this work were based on a computational grid having a nondimensional element size of $l^* = 4$. Though some error exists, we feel the predictions are reasonably well resolved.

IV. Explosively Driven Valve Operation

Results are given in this section that describe explosive actuation of the nitrogen cartridge valve. To this end, values for two model parameters are first correlated with a small number of experiments. The burning rate is chosen so that the predicted pressure rise matches

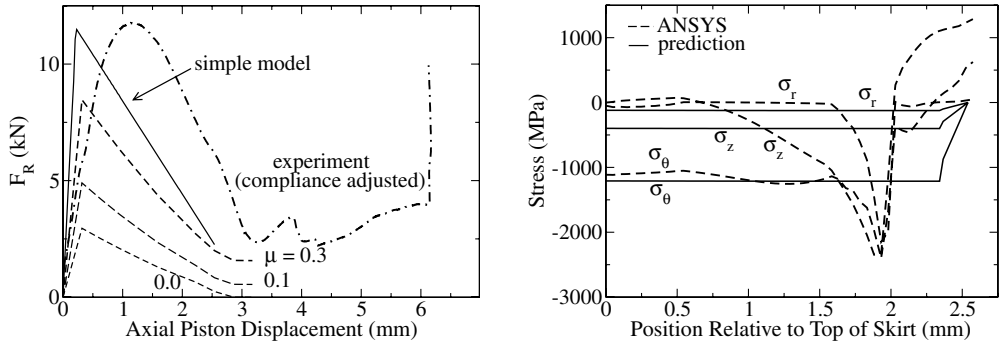

Fig. 8 a) FEA predictions for the variation in resistive force with piston displacement. b) Piston skirt-housing interface stress distribution predicted by the simple deformation model and the FEA simulation for 25% piston insertion.

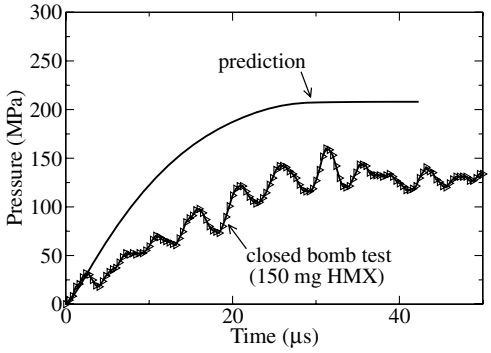

Fig. 10 Comparison of predicted and measured pressure history for a 1 cm^3 combustion bomb experiment for HMX.

closed bomb combustion data for HMX thereby establishing a proper combustion timescale; this is accomplished by adjusting the number of burning grains produced by bridgewire ignition. Likewise, the friction coefficient value for the skirt region of the valve is chosen based on an explosively actuated valve experiment to properly establish a baseline valve operation timescale. Values for these parameters are among the most difficult to directly measure in transient combustion tests. Having determined values for these parameters, a comprehensive parametric study is performed to characterize how variations in key model parameters, including those important from a design perspective, such as explosive mass and valve geometry, affect piston insertion and valve performance.

A. Combustion Bomb Experiment

For the combustion bomb experiment, an actuator containing 150 mg of HMX is fired into a rigid 1 cm^3 vessel while pressure-time data are simultaneously recorded by a transducer. Figure 10 gives the measured pressure history and that predicted by the model for this experiment. The burning rate coefficients b and n used for the model prediction were taken from the literature for HMX [21], and the number of burning grains N was adjusted to match the measured pressure rise timescale. This approach is reasonable as the number of burning grains is difficult to estimate a priori. The value $N = 10,000$ grains was used in the simulation, corresponding to a burning grain size of approximately 400 μm in diameter, which compares to a typical HMX crystal grain size of approximately 50 μm.

Oscillations exist in the measured data, possibly due to either burn instabilities or reflected pressure waves within the vessel; the average frequency of these oscillations is approximately 100 kHz. This measured frequency agrees well with an estimate for the frequency of acoustic reflections off the vessel's walls of approximately 95 kHz, which is based on a characteristic vessel length of 1.27 cm and an acoustic wave speed of 1200 m/s. This agreement suggests that compressible wave propagation within the vessel is likely responsible for the measured pressure oscillations, but additional analysis is needed to firmly substantiate this assertion. Though the predicted peak pressure ($\approx$200 MPa) overshoots the measured value within the closed bomb ($\approx$150 MPa), matching the peak pressure is not as critical to the model as matching the pressurization timescale. Possible reasons for the discrepancy in peak pressure include incomplete HMX combustion and nonideal product gas behavior at elevated pressure and temperature. Compressibility factor estimates for key gas product species (N_2, CO, and H_2O) at reduced pressures within the range of 10–50, and reduced temperatures within the range of 10–30, exceed unity ($\approx$1.1–1.3), indicating a departure from ideal gas behavior. However at fixed volume and combustion temperature, such values would tend to increase the pressure above that predicted here; as such, incomplete HMX combustion may be a more probable cause for the discrepancy. Experiments also indicate that pressure measurements are highly dependent on the location of the pressure transducer within the bomb which is also consistent with spatially dependent fields.

B. Baseline Valve Experiment

This subsection characterizes the baseline operation of a nitrogen cartridge valve and demonstrates that important experimental quantities can be predicted by adjusting a single model parameter (μ_s). Baseline parameters used in the simulations are listed in Table 3, where r_{ho} is the outer radius of the housing, r_{hi} is the inner radius of the housing in the constant radius bore region, and tk is the piston skirt thickness. The parameters $\hat{L}_p$, tk, r_{ho}, r_{hi}, and θ define the initial valve geometry. The value of μ_s was chosen to predict the overall valve operation timescale. Whereas a larger value of friction coefficient was used to replicate the MTS tests, Jones et al. [11], have shown that smaller values are appropriate for dynamic valve actuation. As such, we chose a value of $\mu_s = 0.4$, and determined μ_b by ad hocly requiring that the ratio $\mu_s/\mu_b = 4.5$ be identical to that determined by the MTS tests. The piston stroke distance for all simulations performed in this work is 0.635 cm.

A stiff ODE solver contained in the package LSODE is used to numerically integrate Eq. (16). The domain $0 \le \xi \le \hat{L}_p$ was numerically divided into 20 equally spaced intervals, and the integrals given by Eq. (20) were numerically approximated using the trapezoidal rule. Numerical experiments have shown that the results are insensitive to increasing the number of intervals beyond 20. The domain within the skirt region of the valve decreases as the piston is displaced into bore, whereas the domain within the bore increases.

Table 3 Parameter values used for the HMX driven baseline valve simulation

Actuator and expansion chamber model			Piston–housing deformation model		
Parameter	Value	Units	Parameter	Value	Units
A_1	0.5	cm^2	E_h	214	GPa
A_e	0.112	cm^2	E_p	200	GPa
b	2.926×10^{-5}	Pa$^{-0.8}$ cm/s	H_h	0.35	——
h	1.25×10^6	g/s^3/K	H_p	0.0	——
m_p	8.0	g	σ_{h0}	344.7	MPa
n	0.8	——	σ_{p0}	1089	MPa
N	10,000	grains	ν_h	0.3	——
m_{s0}	150.0	mg	ν_p	0.3	——
P_{crit}	55.0	MPa	μ_s	0.4	——
T_0	288	K	μ_b	0.089	——
T_w	288	K	$\hat{L}_p$	2.54	mm
V_1	0.0786	cm^3	tk	0.6429	mm
V_{20}	0.75	cm^3	r_{ho}	12.7	mm
V_{s0}	0.0786	cm^3	r_{hi}	5.969	mm
α	0.60	——	θ	9	Degrees
ϵ	0.60	——			
ρ_{g1_0}	6.202×10^{-6}	g/cm^3			
ρ_s	1.91	g/cm^3			

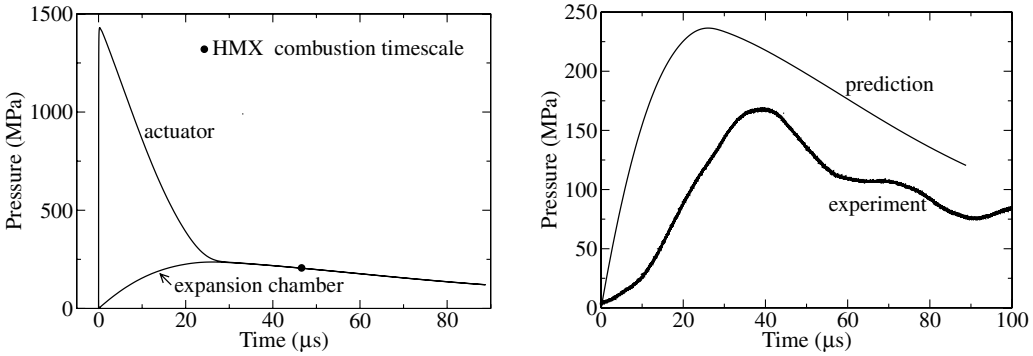

a) b)

Fig. 11 Baseline valve predictions: a) actuator and expansion chamber pressure history; b) comparison of predicted and measured expansion chamber pressure history.

Numerical error may result when the domain size becomes equal to, or smaller than, the integration interval size. This error is likely small because the resistive force from the bore region dominates the net resistive force for large piston displacements. The nonlinear algebraic system defined by Eq. (34) was solved using a standard Newton–Raphson method (DGESVX) contained in the LAPACK subroutine package. Numerical implementation of the elastic–plastic model was validated against the predictions given in [18]. All simulations were performed on a Linux workstation having an INTEL Pentium IV, 1.3 GHz processor with 528 Mb RAM. The average computational run time for a simulation was approximately 45 min.

Figure 11a gives the predicted pressure history in both the actuator and expansion chamber for the baseline case. The actuator pressure rapidly increases, reaching a maximum value of approximately 1430 MPa in 1 μs, whereas the expansion chamber pressure increases more slowly because of choked flow through the actuator port induced by the large pressure difference. The pressures equilibrate approximately 30 μs following ignition, and subsequently decrease due to the combined effect of volume expansion from piston motion and heat transfer to the surroundings. Figure 11b compares the predicted and experimentally measured expansion chamber pressure histories; no data are available for actuator pressure. The histories exhibit the same trends, though the predicted peak pressure is larger than the measured value, likely due to incomplete HMX combustion and transducer positioning within the chamber. As with the closed bomb experiment, accurately predicting the pressurization timescale is more important than the peak pressure, provided the discrepancy is not too large. The measured history also indicates the existence of weak oscillations during piston motion; the reason for these oscillations is unclear, but may be due to gas dynamic wave reflections within the chamber or burn instabilities. Complete HMX combustion is predicted to occur approximately 46 μs following ignition.

Figure 12a gives a comparison between the predicted and measured piston velocity histories for the baseline case. A VISAR (velocity interferometer system for any reflector) system was used to experimentally determine piston velocity. The valve used to perform these measurements was identical to the actual valve except that the diaphragm and piston stops were removed, and the bore tube was extended and opened to the atmosphere to provide the VISAR with optical access to the bottom surface of the piston. The predicted and measured histories agree well. The piston reaches a peak velocity near 200 m/s as it exits the bore tube extension. The piston stroke time, assuming that the stops were in place, is approximately 90 μs, at which time the piston velocity is approximately 150 m/s. These results suggest that the piston is significantly overdriven by 150 mg of HMX based on the minimal piston kinetic energy required to puncture the diaphragm established by the MTS tests.

Figure 12b gives the predicted piston force histories for the baseline case. The sum of the expansion chamber pressure force and the deformation induced resistive force (the magnitude of this force is shown in the figure) gives the net force acting on the piston. The pressure force history is directly proportional to the pressure history, and the resistive force history follows a similar trend to the inert, quasi-static FEA predictions in that it monotonically increases to a maximum value, and then sharply decreases until the piston is fully inserted into the bore. Following complete piston insertion, the resistive force is nearly constant as there is no additional geometrical interference, though it slightly decreases due to diminishing piston–housing interference induced by decreasing expansion chamber pressure. The pressure force always exceeds the resistive force for this baseline case. The predicted net piston force history is complex because of the wide range of physical phenomena accounted for by the model; as such, it would be exceptionally difficult to estimate the net force history profile for modified valve configurations in the absence of modeling.

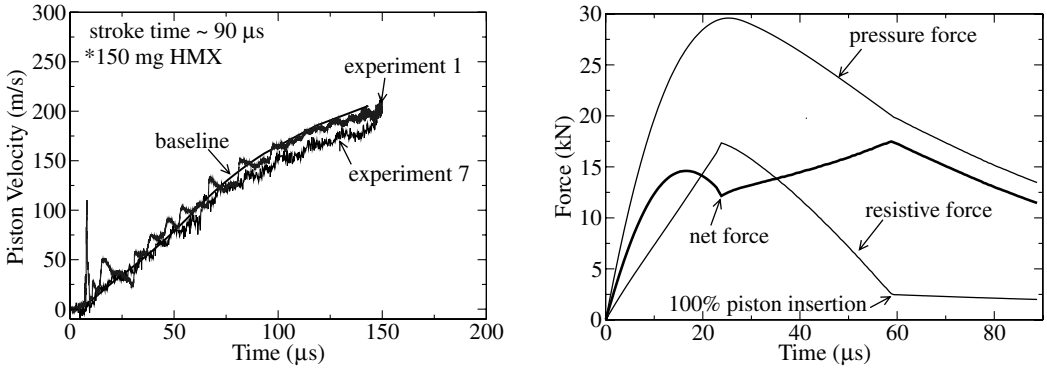

a) b)

Fig. 12 Baseline valve predictions: a) comparison of predicted and measured piston velocity history; b) piston force history.

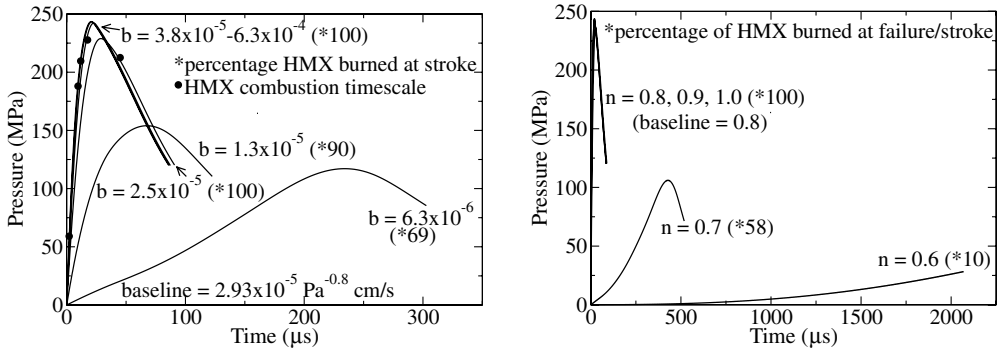

Fig. 13 The predicted variation in expansion chamber pressure with burning rate a) prefactor and b) exponent.

Lastly it is instructive to decouple the deformation and combustion models to determine at what internal pressure the piston and housing begin to plastically deform. To this end, a constant internal pressure is imposed as the piston is displaced into the bore. The analysis reveals that the piston skirt rapidly yields and undergoes uncontained plasticity, even in the absence of internal pressure, whereas the housing requires an internal pressure of approximately 15 MPa to first yield during piston insertion, and requires 200 MPa for uncontained plasticity. For the baseline case, the maximum pressure in the expansion chamber is approximately 235 MPa, which indicates a fully plastic housing; such a condition might imply structural failure of the valve. However this predicted peak pressure far exceeds the measured value of approximately 175 MPa. Using the measured peak pressure value in the analysis, the housing would not experience uncontained plasticity. While the inclusion of structural plastic deformation may be used to determine the likelihood of device failure due to uncontained plastic flow, it is sensitive to expansion chamber pressure.

V. Parametric Analysis

A key capability of the comprehensive model is its ability to provide quick, inexpensive estimates for how design modifications affect valve performance. In this section, we first give results of a parametric analysis intended to illustrate how variations in the explosive burning rate r_b, and the friction coefficient μ_s, affect baseline valve operation. It is important to establish model sensitivity to these parameters as they contain significant uncertainty, particularly for highly dynamic explosive valve actuation. We then give predictions for how variations in explosive mass and valve geometry affect performance as they are important from a design perspective. For this analysis, the parameter of interests is independently varied while all remaining parameters are fixed at their baseline values listed in Table 3.

A. Parameters Containing Significant Uncertainty

Figures 13a and 13b illustrate expansion chamber pressure sensitivity to independent variations in the burning rate prefactor b and exponent n, respectively. For this study, the prefactor was varied over the range $6.3 \times 10^{-6} \le b \le 6.3 \times 10^{-4}$ Pa$^{-0.8}$ cm/s [$1 \times 10^{-6} \le b \le 1 \times 10^{-4}$ (dyne/cm^2)$^{-0.8}$ cm/s], and the exponent was varied over the range $0.6 \le n \le 1.0$. All history plots are given up to the time of piston stroke. As seen in Fig. 13a for $b = 6.3 \times 10^{-6}$ Pa$^{-0.8}$ cm/s, the propellant slowly burns until a maximum expansion chamber pressure near 125 MPa is obtained approximately 300 μs following ignition just before stroke; the explosive is only 69% consumed at this time. This piston stroke time is much greater than that for the baseline case (90 μs). As the value of b increases, the maximum pressure increases and the stroke time decreases. For $b = 1.3 \times 10^{-5}$ Pa$^{-0.8}$ cm/s, the piston again successfully strokes, with 90% of the explosive consumed. Further increases in b produce little change in pressure history, and all explosive is consumed. The pressure history is invariant for large burning rates due to mass choking through the actuator port. The explosive burning times decrease from 65 μs for $b = 2.5 \times 10^{-5}$ Pa$^{-0.8}$ cm/s to 0.58 μs for $b = 6.3 \times 10^{-4}$ Pa$^{-0.8}$ cm/s. Similar qualitative trends are predicted for the pressure sensitivity to n. It is noted that the burning rate is sufficiently slow for $n = 0.6$ to cause the piston velocity to vanish before stroke, approximately 2100 μs following ignition, at which point only 10% of the explosive is burned. As n increases, the maximum pressure increases and the stroke time decreases. The pressure histories become indistinguishable for exponents within the range $0.8 \le n \le 1.0$, even though propellant burning times continue to decrease. Similar predictions are obtained by varying the number of burning grains N, which are omitted here for brevity.

Figure 14a gives predicted piston velocity histories for skirt friction coefficient values within the range $0 \le \mu_s \le 1$. Corresponding values for the bore friction coefficient are chosen so that $\mu_s/\mu_b = 4.5$ as with the baseline case. The value $\mu_s = 0$

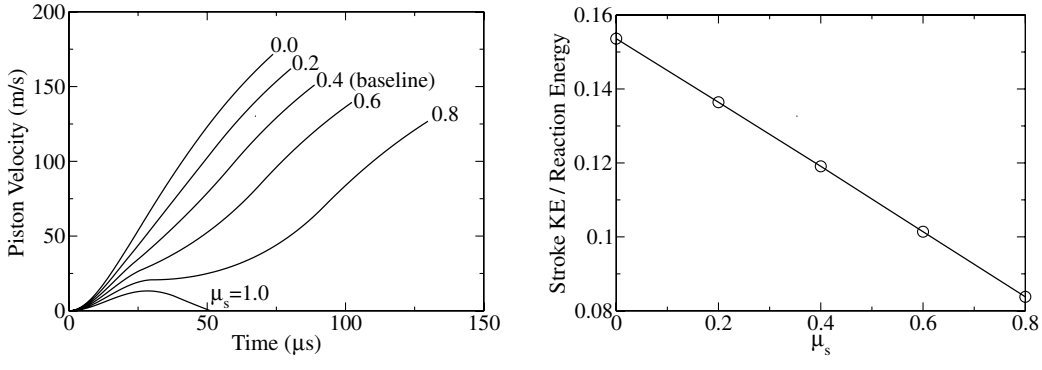

Fig. 14 Predicted variation in a) piston velocity history, and b) piston kinetic energy at stroke, with skirt friction coefficient. The piston kinetic energy is scaled by the HMX combustion energy.

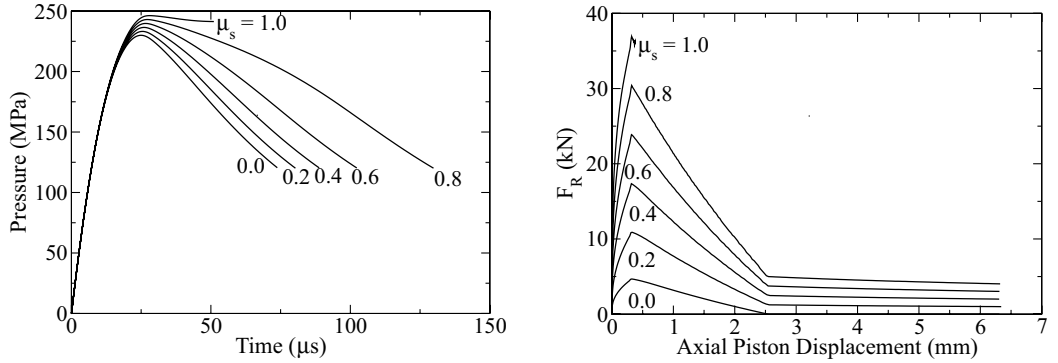

a) b)

Fig. 15 Predicted variation in a) expansion chamber pressure history, and b) resistive force-piston displacement profile, with skirt friction coefficient.

results in the largest piston stroke velocity (≈170 m/s) and the fastest stroke time (≈73 μs). The velocity histories for $\mu_s = 0.8$ and 1.0 include a local maximum at approximately 30 μs following ignition where the resistive force balances the driving pressure force. For $\mu_s = 1.0$, the magnitude of the resistive force is sufficiently large to overcome the pressure force and decelerate the piston until its velocity vanishes at approximately 50 μs. Figure 14b gives corresponding predictions for the variation in piston kinetic energy at stroke with μ_s. Here, the piston kinetic energy is scaled by the reaction energy; a linear relation results. The history for $\mu_s = 1.0$ is ignored because the piston velocity vanishes before stroke. Note that even for $\mu_s = 0.0$, the system is only 15% efficient in converting reaction energy into piston kinetic energy at stroke. The remaining energy can be accounted for by heat transfer, volume expansion, and stored combustion product internal energy when the piston strokes. It is likely that irreversible phenomena not accounted for by the model will further reduce this efficiency in practice.

Figure 15a gives the predicted variation in expansion chamber pressure history with μ_s. The initial pressure response is largely identical for all values of μ_s due to piston inertia; a finite time is required for the piston to begin moving which is independent of μ_s. Larger friction coefficients reduce the volume expansion rate and result in broader pressure history profiles. Figure 15b gives corresponding variations in resistive force with piston displacement. The profiles are qualitatively similar, though the peak force increases with μ_s. Note that the resistive force does not vanish for $\mu_s = 0$ because of piston taper within the skirt region of the valve; the axial resistive force balances the axial component of the integrated expansion chamber pressure force within this region.

B. Parameters of Design Importance

The explosive mass used in the valve can greatly affect its performance. If too little mass is used, the explosive may provide insufficient piston energy for proper valve operation, whereas too much mass may result in excessive valve deformation and catastrophic failure. Figure 16a gives predictions for the variation in expansion chamber pressure history with explosive mass. Here, we

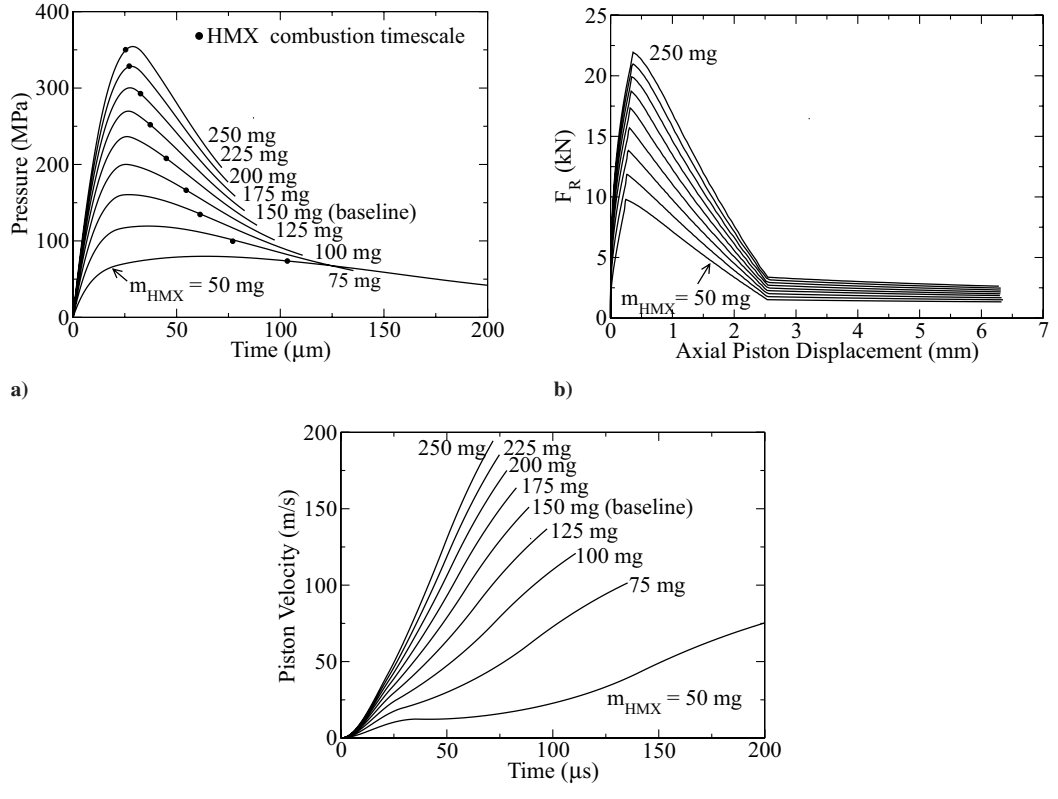

a) b) c)

Fig. 16 Predicted variation in valve performance with explosive mass: a) expansion chamber pressure history; b) resistive force-piston displacement profile; and c) piston velocity history.

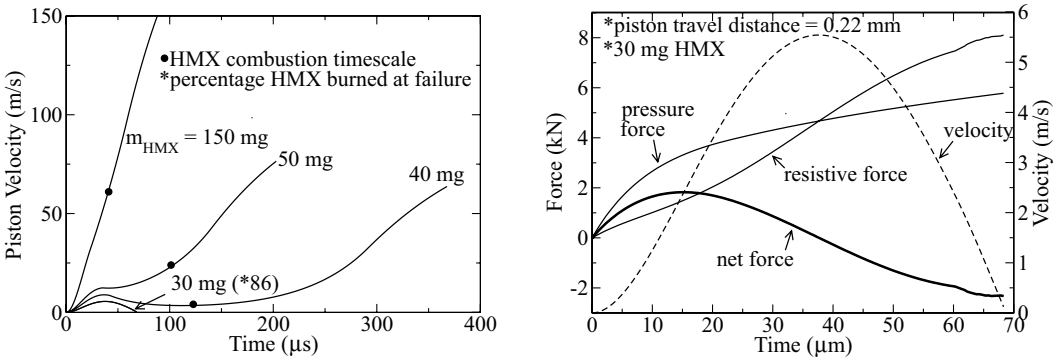

a) b)

Fig. 17 Predictions for a reduced explosive mass that results in vanishing piston velocity: a) piston velocity history; b) piston force history.

take $50 \leq m_s \leq 250$ mg HMX, where $m_s = 150$ mg is the baseline value. For all cases, an initially slow pressure rise is predicted that is largely governed by the mass flow rate of combustion products through the actuator port. Smaller amounts of explosive mass reduce the driving actuator pressure and increase the operation time of the valve. Stroke times range from 202 μs for $m_s = 50$ mg, to 67 μs for $m_s = 250$ mg. The lower actuator pressure also increases the explosive burning time, which ranges from 116 μs for $m_s = 50$ mg, to 29 μs for $m_s = 250$ mg. Note that as explosive mass increases, the burning time asymptotically approaches a minimum value near 25 μs that coincides with the time to peak expansion chamber pressure. Figure 16b gives the variation in resistive force with piston displacement for 25 mg increments of explosive mass over the range $50 \leq m_s \leq 250$ mg. Larger explosive mass results in higher expansion chamber pressure; consequently, greater interference between the piston and housing is predicted during insertion. The corresponding predicted piston velocity histories are shown in Fig. 16c. Piston stroke velocities vary from 75 m/s for $m_s = 50$ mg, to 195 m/s for $m_s = 250$ mg.

There exists a minimal explosive mass that will not drive the piston to stroke completion. To characterize this threshold, Fig. 17a gives piston velocity histories for $m_s = 30, 40, 50$, and 150 mg. The piston successfully strokes for all cases except $m_s = 30$ mg as the piston velocity vanishes approximately 70 μs following ignition. The force histories shown in Fig. 17b summarize the piston dynamics for this exceptional case. As seen in the figure, the piston accelerates for approximately 40 μs as the expansion chamber pressure force exceeds the resistive force, but then decelerates as the resistive force dominates the pressure force. The maximum piston velocity predicted for this case is 5.5 m/s. The piston velocity vanishes approximately 68 μs following ignition. The explosive mass threshold required for the valve to properly function will be greater than that predicted here as additional piston energy is needed to cleanly puncture the diaphragm. It should also be noted that the pressure dependent burn model used in this analysis may be inadequate for describing combustion near quenching conditions.

We now briefly describe how variations in valve geometry can affect performance. To this end, we separately examine the effects of piston skirt thickness, housing thickness, and skirt taper angle. Because housing thickness varies over the tapered region of the valve, we define this thickness as the difference between the uniform outer radius of the housing and the uniform bore radius, the latter of which is fixed for this study at its baseline value. Figures 18a–18d illustrate the variation in piston resistive force and velocity with both skirt and housing thickness, respectively, where the dimensionless ratio t^* is defined as the corresponding thickness divided by its baseline value. The resistive force-piston displacement profiles are qualitatively similar to the baseline case. The magnitude of the resistive force is sensitive to variations in piston skirt thickness, but is largely insensitive to variations in housing thickness. As seen in Fig. 18a, a peak resistive force near 40 kN occurs for a dimensionless piston skirt thickness of $t^* = 4.0$; the large force generated by deformation of the thick skirt is sufficient to cause the piston velocity to vanish before stroke, as seen in Fig. 18b. The lack of model sensitivity to variations in housing thickness is due, in part, to the mechanical properties of the piston which is modeled as elastic-perfectly plastic. Thicker housings may be required for pistons that exhibit strong strain hardening behavior, though such pistons may be of limited use in practice. These results suggest that careful attention should be placed on piston design.

Lastly proper selection of the skirt taper angle is an important design consideration: small taper angles may result in excessive blowby of combustion product gas past the piston, whereas large taper angles will require considerable energy for piston insertion. Figure 19 illustrates how skirt taper angle affects the resistive force for selected values within the range $0 \leq \theta \leq 15$ deg. To this end, we have fixed the friction coefficients in both the skirt and bore regions of the valve at their baseline values, with the exception of $\theta = 0$ for which we have taken $\mu_s = \mu_b = 0.089$, but realize that these coefficients will likely depend on θ. The predictions are qualitatively similar, though the peak force increases with skirt angle. It is important to note that even though the peak resistive force increases with θ, piston velocity is not significantly affected; the piston stroke velocity varies from 164 m/s for $\theta = 0$ deg to 150 m/s for $\theta = 15$ deg. This predicted insensitivity likely results from the piston being overdriven by the 150 mg of HMX. It should be also noted that the simple model is less valid for larger skirt angles as deformations become large and stresses become increasingly three dimensional.

VI. Conclusions

A comprehensive model was formulated that mathematically describes all key features of explosive valve actuation including pressure dependent burning of solid explosive to form combustion product gases within an actuator, flow of product gases from the actuator to a gas expansion chamber due to a pressure imbalance, and work performed by high pressure gases within the expansion chamber to insert a tapered piston into a constant diameter bore which is necessary to enable the flow of stored gas within the valve. The model is an improvement and extension of existing models used to describe explosively and pyrotechnically actuated devices in that it rationally couples pressure dependent explosive combustion to the deformation work required to insert the piston into the housing bore. The valve deformation submodel is analytically based on pressure vessel theory, and accounts for quasi-steady, elastic–plastic deformation of the piston and housing in a mechanically consistent manner, including the effects of linear strain hardening and internal gas pressure.

The deformation submodel is easily correlated with inert, quasi-static valve compression tests to estimate work requirements by numerically integrating resistive force-displacement data. These tests indicate that piston skirt insertion into the bore dominates the valve work requirements, accounting for approximately 62% of the total work (24.14 J); the remainder of the work accounts for displacement of the fully inserted piston through the remainder of the

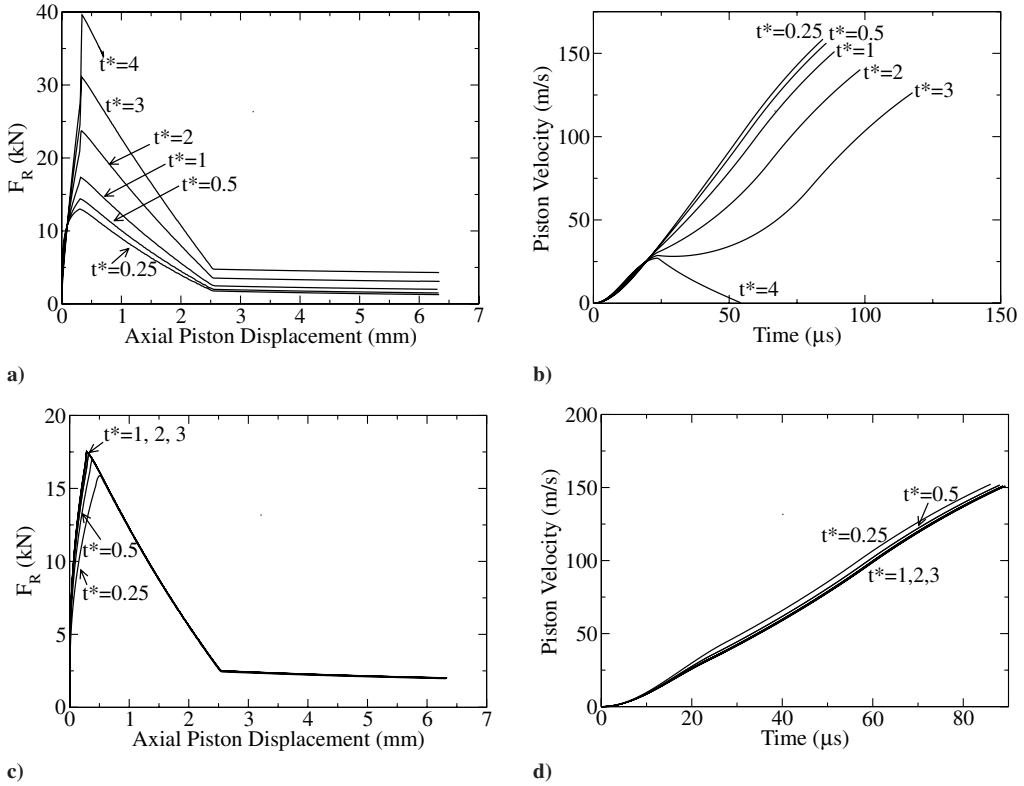

Fig. 18 Predictions for the variation in valve performance with geometry: a), b) piston thickness; c), d) housing thickness.

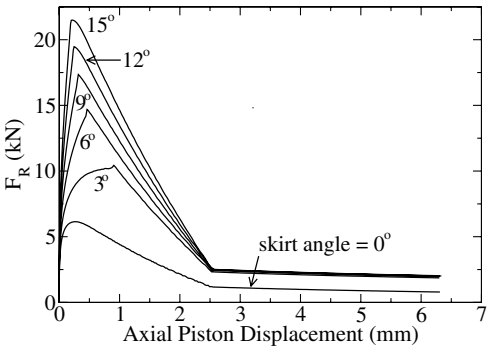

Fig. 19 Predicted variation in resistive force with piston skirt taper angle.

bore (38%) and diaphragm puncture (10%). Inert, quasi-static predictions from a finite-element analysis (FEA) indicate that significant bending stresses develop within the piston skirt that are unaccounted for by the deformation submodel; these stresses result from large deformations occurring in the vicinity of the housing corner that connect the tapered region of the expansion chamber to the bore. The FEA predictions further indicate that a relatively low resistive force exists once the piston is fully displaced into the bore, which agrees well with compression test data, and that the assumptions of uncontained plasticity within the piston and contained plasticity within the housing are reasonable. The effect of complex piston bending induced by the housing corner is implicitly accounted for by the deformation submodel through the use of a different constant friction coefficient within the tapered skirt and uniform bore regions of the valve housing. Resistive force predictions for piston displacement given by the deformation submodel agree well with the FEA predictions.

The comprehensive model was demonstrated by applying it to an HMX ($C_4H_8N_8O_8$) driven nitrogen cartridge valve. The number of burning grains used with the combustion model was first correlated with closed bomb combustion data for HMX, and the friction coefficients were chosen so that the model reasonably reflects the operation time for a baseline valve configuration ($\approx$90 μs). Though not addressed in this paper, it may be possible to estimate these parameters in the absence of experimental data using well-motivated plausibility arguments and published data. Having fixed these parameters, the model accurately predicts measured expansion chamber pressure and piston velocity histories. Results of an extensive parametric study indicate that the piston is significantly overdriven by combustion of 150 mg of HMX used with the baseline valve as the final piston kinetic energy ($\approx$90 J) far exceeds that required to successfully puncture the valve diaphragm ($\approx$2.1 J); as such, there exists little variation in valve performance as explosive mass is slightly reduced. By varying valve geometry, including piston skirt thickness and taper, and housing thickness, it was shown that valve performance is considerably more sensitive to piston geometry than housing thickness; as such, care should be exercised when making design choices about piston geometry. It is anticipated that this model will prove useful in identifying optimal configurations for explosively actuated devices based on suitably defined performance measures. These configurations can then be further explored by performing a reduced set of detailed finite-element simulations and experiments.

Acknowledgments

The authors gratefully acknowledge both the Louisiana Space Consortium (LaSpace) and the Engineering Sciences and Applications Division, Gas Transfer Systems Group, Los Alamos National Laboratory, for supporting this work. They also thank the Civil Engineering Department, Louisiana State University, for the use of their MTS machine to perform the quasi-static valve compression tests.

References

[1] Bement, L. J., "Functional Performance of Pyrovalves," *Journal of Spacecraft and Rockets*, Vol. 34, No. 3, 1997, pp. 391–396.

[2] Bement, L. J., "Pyrotechnic System Failures; Causes and Prevention," NASA TM 100633, June 1988.

[3] Bement, L. J., and Schimmel, M. L., "Determination of Pyrotechnic Functional Margin," *Proceedings of the 1991 SAFE Symposium*, SAFE Association, Creswell, OR, 1991.
[4] Bement, L. J., Schimmel, M. L., Karp, H., and Magenot, M. C., "Development and Demonstration of an NSI-Derived Gas Generating Cartridge," *Proceedings of the 1994 NASA Pyrotechnic Systems Workshop*; NASA Conf. Pub. 3258.
[5] Bement, L. J., and Schimmel, M. L., "A Manual on Pyrotechnic Design, Development, and Qualification," NASA TM 110172, June 1995.
[6] Decroix, M., Quintana, D., Burnett, D., Tafoya, J. I., and Tafoya, J. M., "Investigation of Actuation Dynamics in an Explosively Actuated Valve Using a Gas Gun," AIAA Paper 2005-4036, July 2005.
[7] Rossi, C., Rouhani, M., and Esteve, D., "Prediction of the Performance of a Si-Micromachined Microthruster by Computing the Subsonic Gas Flow Inside the Thruster," *Sensors and Actuators A*, Vol. 87, No. 1–2, 2000, pp. 96–104.
[8] Rossi, C., Conto, T., Esteve, D., and Larangot, B., "Design, Fabrication, and Modelling of MEMS-Based Microthrusters for Space Application," *Smart Materials and Structures*, Vol. 10, Dec. 2001, pp. 1156–1162.
[9] Orieux, S., Rossi, C., and Esteve, D., "Compact Model Based on a Lumped Parameter Approach for the Prediction of Solid Propellant Micro-Rocket Performance," *Sensors and Actuators A*, Vol. 101, No. 3, 2002, pp. 383–391.
[10] Rossi, C., Larangot, B., Lagrange, D., and Chaalane, A., "Final Characterizations of MEMS-Based Pyrotechnical Microthrusters," *Sensors and Actuators A*, Vol. 121, No. 2, 2005, pp. 508–514.
[11] Emery, A. F., Deckers, S., and Jones, B. K., "Design and Analysis of Explosively Actuated Valves: The Interaction of the Plunger and the Housing," *Journal of Mechanical Design*, Vol. 117, No. 2, 1995, pp. 215–220.
[12] Jones, B. K., Emery, A. F., Hardwick, M. F., and Ng, R., "Analysis of Explosively Actuated Valves," *Journal of Mechanical Design*, Vol. 116, No. 3, 1994, pp. 809–815.
[13] Ng, R., and Kwon, D. M., "The Use of MAVIS II to Integrate Modeling and Analysis of Explosive Valve Interactions," Sandia National Laboratories Tech. Rept. SAND-97-8645C, Livermore, CA, Dec. 1998.
[14] Gonthier, K. A., and Powers, J. M., "Formulation, Predictions, and Sensitivity Analysis of a Pyrotechnically Actuated Pin Puller Model," *Journal of Propulsion and Power*, Vol. 10, No. 4, 1993, pp. 501–507.
[15] Gonthier, K. A., Kane, T. J., and Powers, J. M., "Modeling Pyrotechnic Shock in a NASA Standard Initiator Driven Pin Puller," AIAA Paper 94-3054, 1994.
[16] Tarver, C., Chidester, S., and Nichols, A., "Critical Conditions for Impact and Shock Induced Hot Spots in Solid Explosives," *Journal of Physical Chemistry*, Vol. 100, No. 14, 1996, pp. 5794–5799.
[17] Lee, H., "Unsteady Gasdynamics Effects in Pyrotechnic Actuators," *Journal of Spacecraft and Rockets*, Vol. 41, No. 5, 2004, pp. 877–886.
[18] Eraslan, A. N., and Akis, T., "Deformation Analysis of Elastic-Plastic Two Layer Tubes Subject to Pressure: an Analytical Approach," *Turkish Journal of Engineering and Environmental Sciences*, Vol. 28, 2004, pp. 261–268.
[19] Lubliner, J., *Plasticity Theory*, Macmillan, New York, 1990.
[20] Braud, A. M., Gonthier, K. A., and Decroix, M. E., "Performance Modeling for Explosively Actuated Valves," AIAA Paper No. 2005-3843, 2005.
[21] Atwood, A. I., Boggs, T. L., Curran, P. O., Parr, T. P., Hanson-Parr, D. M., Price, C. F., and Wiknich, J., "Burning Rate of Solid Propellant Ingredients, Part 1: Pressure and Initial Temperature Effects," *Journal of Propulsion and Power*, Vol. 15, No. 6, 1999, pp. 740–747.

S. Son
Associate Editor